1

Neutrino Geoscience: Review, Survey, Future Prospects

W. F. McDonough^{1,2,3,*} and H. Watanabe¹

ABSTRACT

The Earth's surface heat flux is 46 ± 3 TW (terawatts, 10^{12} watts). Although many assume we know the Earth's abundance and distribution of radioactive HPEs (i.e., U, Th, and K), estimates for the mantle's heat production varying by an order of magnitude and recent particle physics findings challenge our dominant paradigm. Geologists predict the Earth's budget of radiogenic power at 20 ± 10 TW, whereas particle physics experiments predict $15.3^{+4.9}_{-4.9}$ TW (KamLAND, Japan) and $38.2^{+13.6}_{-12.7}$ TW (Borexino, Italy). We welcome this opportunity to highlight the fundamentally important resource offered by the physics community and call attention to the shortcomings associated with the characterization of the geology of the Earth. We review the findings from continent-based, physics experiments, the predictions from geology, and assess the degree of misfit between the physics measurements and predicted models of the continental lithosphere and underlying mantle. Because our knowledge of the continents is somewhat uncertain $(7.1^{+2.1}_{-1.6}$ TW), models for the radiogenic power in the mantle (3.5–32 TW) and the bulk silicate Earth (BSE; crust plus mantle) continue to be uncertain by a factor of ~10 and ~4, respectively. Detection of a geoneutrino signal in the ocean, far from the influence of continents, offers the potential to resolve this tension. Neutrino geoscience is a powerful new tool to interrogate the composition of the continental crust and mantle and its structures.

1.1. INTRODUCTION

Core-mantle evolution involves understanding Earth's differentiation processes, which established the present-day distribution of the HPEs, and its dynamic consequences (i.e., the radiogenic heat left in the mantle powering mantle convection, plate tectonics, and the geodynamo). The energy to drive the Earth's engine comes from two different sources: primordial and radiogenic.

Corresponding author: William McDonough, mcdonoug@umd.edu.

Primordial energy represents the kinetic energy inherited during accretion and core formation. Radiogenic energy is the heat of reaction from nuclear decay. We do not have a constraint on the proportion of these different energy sources driving the present-day Earth's dynamics. In turn, this means that we do not have sufficient constraint on the thermal evolution of the planet, aside from first-order generalities. You might ask, is this important? We ask the question – how much energy (and time) is left to keep the Earth habitable?

We understand that the Earth started out hot due to abundant accretion energy, the gravitational energy of sinking metal into the center, a giant impact event for the formation of the Earth's Moon, and energy from short-lived (e.g., ²⁶Al and ⁶⁰Fe) and long-lived (K, Th, and U) radionuclides. From this hot start the planet should quickly lose some of its initial energy, although

Core-Mantle Co-Evolution: An Interdisciplinary Approach, Geophysical Monograph 276, First Edition. Edited by Takashi Nakagawa, Taku Tsuchiya, Madhusoodhan Satish-Kumar, and George Helffrich. © 2023 American Geophysical Union. Published 2023 by John Wiley & Sons, Inc.

DOI: 10.1002/9781119526902.ch01

¹Research Center for Neutrino Science, Tohoku University, Sendai, Miyagi, Japan

²Department of Earth Sciences, Tohoku University, Sendai, Miyagi, Japan

³Department of Geology, University of Maryland, College Park, MD, USA

the amount and rate are unknowns. There are many significant unknowns regarding the thermal evolution of the Earth: (1) the nature and presence (or absence) and lifetime of an early atmosphere, which has a thermal blanketing effect; (2) the compositional model for the Earth, particularly the absolute abundances of the HPEs (K, Th, and U); (3) the cooling rate of the mantle (present-day estimates: 100 ± 50 K/Ga); and (4) the rate of crust formation and thus extraction of HPEs from the mantle.

The recent recognition (Krauss et al., 1984) and subsequent detection (Araki et al., 2005) of the planet's geoneutrino emission have opened up a new window into global scale geochemistry of the present-day Earth. The measurement of this flux presents Earth scientists with a transformative opportunity for new insights into the composition of the Earth and its energy budget. For the most part, solid Earth geophysics measures and parameterizes the present-day state of the planet. In contrast, solid Earth geochemistry measures and parameterizes its time-integrated state, mostly on a hand sample scale and then extrapolates these insights to larger scales. The advent of measuring the Earth's geoneutrino flux allows us, for the first time, to get a global measure of its present-day amount of Th and U.

This chapter is organized as follows: we provide the rationale for the field of neutrino geoscience and define some terms (section 1.2). We review the existing and developing detectors, the present-day detection methods, and future technologies (section 1.3). We discuss the latest results from the physics experiments (section 1.4). We present the range of compositional models proposed for the Earth (section 1.5) followed by a discussion of the geological prediction of the geoneutrino fluxes at various detectors (section 1.6). We finish with a discussion on determining the radioactive power in the mantle (section 1.7) and future prospects (section 1.8).

1.2. NEUTRINO GEOSCIENCE

The field of neutrino geoscience focuses on constraining the Earth's abundances of Th and U and with these data we can determine: (1) the absolute concentration of refractory elements in the Earth and from that determine the BSE's composition (crust plus mantle), and (2) the amount of radiogenic power in the Earth driving the planet's major dynamic processes (e.g., mantle convection, plate tectonics, magmatism, and the geodynamo). These two constraints set limits on the permissible models for the composition of the Earth and its thermal evolutionary history.

First, the refractory elements are in constant relative abundances in all chondrites. There are 36 of these elements (e.g., Al, Ca, Sr, Zr, REE, Th, and U) and by establishing the absolute abundance of one defines all abundances, since refractory elements exist in constant ratios to each other (McDonough & Sun, 1995). Most of these elements are concentrated in the bulk silicate Earth, but not all (e.g., Mo, W, Ir, Os, Re, etc.) and these latter ones are mostly concentrated in the metallic core. Knowing the Earth's abundance of Ca and Al, two of the eight most abundant elements (i.e., O, Fe, Mg, Si, Ca, Al, Ni, and S) that make up terrestrial planets (i.e., 99%, mass and atomic proportions) define and restrict the range of accepted compositional models of the bulk Earth and BSE.

Second, the decay of 40 K, 232 Th, 238 U, and 235 U (i.e., HPE) provides the Earth's radiogenic power, accounts for 99.5% of its total radiogenic power, and is estimated to be 19.9 ± 3.0 TW (1 TW = 10^{12} watts). This estimate, however, assumes a specific BSE model composition (McDonough & Sun, 1995; Palme & O'Neill, 2014). It must be noted that there is no consensus on the composition of the BSE, and so predictions from competing compositional models span from about $10{\text -}38$ TW (Agostini et al., 2020; Javoy et al., 2010). This uncertainty in our present state of knowledge means that the field of neutrino geoscience plays a crucial role in resolving fundamental questions in Earth sciences.

1.2.1. Background Terms

The field of neutrino geoscience spans the disciplines of particle physics and geoscience, including geochemistry and geophysics. The following list of terms are offered to support this interdisciplinary research field.

Alpha (α) decay: a radioactive decay process that reduces the original nuclide (X) by four atomic mass units by the emission of a ${}_{2}^{4}$ He nucleus and reaction energy (Q). Commonly, the α particle is emitted with between 4 and 9 MeV (1 MeV = 10^{6} eV) of discrete kinetic energy. The basic form of α decay is as follows:

Alpha (
$$\alpha$$
) ${}^{A}_{Z}X \rightarrow {}^{A-4}_{Z-2}X' + \alpha + Q$ (1.1)

Beta decay: a radioactive decay process that transforms the original nuclide (X) into an isobar (same mass A) with the next lower proton number (Z) during either electron capture (EC) or β^+ decays or, alternatively, the next higher proton number (Z) during β^- decay. During each decay, there is an exchange of two energetic leptons (i.e., beta particles) and reaction energy (Q). Basic forms are as follows:

Beta Minus
$$(\beta^{-})$$
 ${}^{A}_{Z}X \rightarrow^{A}_{Z+1}X' + e^{-} + \overline{v}_{e} + Q,$
Electron Capture (EC) ${}^{A}_{Z}X + e^{-} \rightarrow^{A}_{Z-1}X' + v_{e} + Q,$
Beta Plus (β^{+}) ${}^{A}_{Z}X \rightarrow^{A}_{Z-1}X' + e^{+} + v_{e} + Q$
(1.2)





Beta particles: first-generation energetic leptons, either matter leptons (electrons and neutrinos: e^- and v_e) or antimatter leptons (positrons and antineutrinos: e^+ and v_e).

Chondrite: an undifferentiated stony meteorite containing chondrules (flash-melted spheres, sub-mm to several mm across), matrix [fine grained (micron scale) aggregate of dust and crystals], and sometimes Ca-Al-inclusions and other refractory phases. They are typically mixtures of silicates and varying amounts of Fe-Ni alloys and classified into groups based on their mineralogy, texture, and redox state. Three dominant groups are the carbonaceous, ordinary, and enstatite type chondrites, from most oxidized to reduced, respectively. Isotopic observations are also used to create a twofold classification of chondrites and related meteorites (i.e., the NC and CC groups). The NC (non carbonaceous) group includes enstatite and ordinary chondrites and is believed to have formed in the inner solar system inside of Jupiter. The CC (carbonaceous) group includes carbonaceous chondrites and is believed to have formed in the outer solar system from Jupiter and beyond. The CI carbonaceous chondrite type (the sole chondrite type lacking chondrules) is considered most primitive because its element abundances matches that of the solar photosphere 1:1 over 6 orders of magnitude, except for the noble and H-C-N-O gases.

Geoneutrinos: naturally occurring electron antineutrinos $(\overline{\nu}_e)$, with the over-bar indicating it is an antimatter particle), mostly, and electron neutrinos (v_e) , much less so, produced during β^- , and [EC and β^+] decays, respectively. The interaction cross-sections, which scale with their energy, for the detectable geoneutrinos (i.e., Th and U) is on the order of 10^{-47} m². Consequently, these particles rarely interact with matter in the Earth. The Earth's geoneutrino flux is $10^{25} \bar{\nu}_e$ s⁻¹ (McDonough et al., 2020). Each neutrino leaving the Earth removes a portion of the Earth's radiogenic heat (Q).

Heat-producing elements (HPEs): potassium, thorium, and uranium (i.e., K, Th, and U, or more specifically ⁴⁰K, 232 Th, 235 U, and 238 U) account for $\sim 99.5\%$ of the Earth's radiogenic heating power.

Inverse Beta Decay (IBD): a nuclear reaction used to detect electron antineutrinos in large underground liquid scintillation detectors that are surrounded by thousands of photomultiplier tubes. The reaction $[\overline{v}_e + p \rightarrow e^+ + n]$ involves a free proton (i.e., H ion) capturing a through going \overline{v}_e and results in two flashes of light close in space and time. The first flash of light involves $e^+ - e^-$ annihilation (order a picosecond following $\overline{v}_e + p$ interaction) and the second flash (\sim 0.2 ms later) comes from the capture by a free proton of the thermalizing neutron. This coincidence of a double light flash in space and time, with the second flash having 2.2 MeV light, reduces the background by a million-fold. This reaction requires the $\overline{\nu}_{o}$ to

carry sufficient energy to overcome the reaction threshold energy of $E_{\overline{\nu}_e}^{thr}=1.8$ MeV. Involving the electron antineutrino restricts us to detecting only antineutrinos from the β^- decays in the ²³⁸U and ²³²Th decay chains.

Major component elements: a cosmochemical classification term for Fe, Ni, Mg, & Si, with half-mass condensation temperatures (T_c) between 1355 and 1250 K. These elements condense from a cooling nebular gas into silicates (first olivine, then pyroxene) and Fe, Ni alloys and together with oxygen represents ≥93% of terrestrial planet's mass (McDonough & Yoshizaki, 2021).

Earth and its parts: the Earth is chemically differentiated. It has a metallic core surrounded by the BSE (aka Primitive Mantle), which initially included the mantle, oceanic and continental crust, and the hydrosphere and atmosphere; the Primitive Mantle is the undegassed and undifferentiated Earth minus the core. The present-day silicate Earth, less the hydrosphere and atmosphere, is made up of the mantle, including its bottom thermally conductive boundary layer (D"), and the top lithosphere; the latter composed of the crust an underlying lithospheric mantle. The lithosphere is the mechanically stiff (i.e., $>10^5$ higher viscosity than the underlying asthenospheric mantle) thermally conductive boundary layer. In the continents, the zone above the Moho (a seismically defined boundary between the crust and mantle) is the continental crust and below the continental lithospheric mantle (CLM). Masses and thicknesses of these domains are listed in Table 1.1.

Moderately volatile elements: a cosmochemical classification term for elements with half-mass condensation temperatures (T_c) between 1250 and 600 K. These elements include the alkali metals (lithophile), some transition metals, all the other metals, less Al, and the pnictogens and chalcogens, less N and O.

Primordial energy: the energy in the Earth from accretion and core formation. Accretion kinetic energy is $\sim 10^{32}$ J, assuming an Earth mass (5.97 \times 10²⁴ kg) and 10 km/s as an average velocity of accreting particles. The gravitational energy of core formation, which translates to heating energy, is $\approx 10^{30}$ J, depending on the assumed settling velocity of a core-forming metal in the growing Earth.

Radiogenic energy: energy of a nuclear reaction (Q) resulting from radioactive decay, given in units of MeV $(1 \text{ MeV} = 10^6 \text{ eV}) \text{ or pJ } (1 \text{ pJ} = 10^{-12} \text{ J}), \text{ where } 1 \text{MeV} =$ 0.1602 pJ. For β decays Q (MeV) = (mass_p - mass_d) × 931.494, with mass_p (mass of parent isotope), mass_d (mass of daughter isotope) in atomic mass units (1 amu = 1.660539×10^{-27} kg = 931.494 MeV), and for α decay, $Q \text{ (MeV)} = (\text{mass}_p - \text{mass}_d - \text{mass}_\alpha) \times 931.494$, where $E = eV/c^2$, or 1 amu = 0.931494 GeV/c².

Refractory elements: a cosmochemical classification term for elements with half-mass condensation

Table 1.1 Mass of the Earth and its Parts

Domain/ reservoir	Thickness km (<u>+</u>)	Mass kg (±)	Citation
Earth	6,371 (+7)	$5.97218 (60) \times 10^{24}$	[1]
Bulk Silicate Earth (BSE)	2,895 (5)	$4.036(6) \times 10^{24}$	[2]
Modern mantle (DM + EM domains) ^b	2,867 (20) ^d	$4.002 (20) \times 10^{24}$	[2]
Oceanic crust ^e	10.5 (4.3)	$0.92 (11) \times 10^{22}$	[3]
Continental crust ^e	40 (9)	$2.22 (26) \times 10^{22}$	[3]
Continental lithospheric mantle (CLM)	115 (80)	$6.3 (0.8) \times 10^{22}$	[3]

^a cited source: 1 = Chambat et al. (2010), 2 = Dziewonski and Anderson (1981), 3 = Wipperfurth et al. (2020)

temperatures (T_c) > 1355 K; they condense at the earliest stage of the cooling of high-temperature nebular gas. These elements are in equal relative proportion ($\pm 15\%$) in chondritic meteorites. In terrestrial planets, many of these elements are classified as lithophile (dominantly coupling with oxygen and hosted in the crust and mantle), or siderophile (dominantly metallically bonded and hosted in the core). The refractory elements include: Be, Al, Ca, Ti, Sc, V, Sr, Y, Zr, Nb, Mo, Rh, Ru, Ba, REE, Hf, Ta, W, Re, Os, Ir, Pt, Th, and U. The core contains $\geq 90\%$ of the Earth's budget of Mo, Rh, Ru, W, Re, Os, Ir, and Pt, about half of its V, and potentially a minor fraction of its Nb.

Surface heat flux: the total surface heat flux from the Earth's interior is reported as 46 ± 3 TW (Jaupart et al., 2015) or 47 ± 2 TW (Davies, 2013). On average the surface heat flux is about 86 mW/m², with that for the continents being 65 mW/m² and for the oceans being 96 mW/m² (Davies, 2013). Energy contributions to this surface flux come from the core (primordial, plus a minor [~1% of the surface total] amount due to inner core crystallization), mantle (a combination of primordial and radiogenic), and crust (radiogenic). Other contributions include negligible additions from tidal heating and crust–mantle differentiation.

1.3. DETECTORS AND DETECTION TECHNOLOGY

Electron antineutrinos (\overline{v}_e) come mostly from the radioactive decays of 40 K, 232 Th, 235 U, and 238 U (i.e., geoneutrinos; Krauss et al., 1984), plus contributions from local anthropogenic sources (i.e., nuclear reactor plants). The Earth emits some 10^{25} s⁻¹ geoneutrinos (McDonough et al., 2020), with 65% coming from β^- decays of 40 K (Fig. 1.1).

The detection of an electron antineutrino uses the IBD reaction: $\overline{v}_e + p \rightarrow e^+ + n$, which has a reaction threshold energy of $E_{\overline{v}_e}^{thr} = 1.806$ MeV.

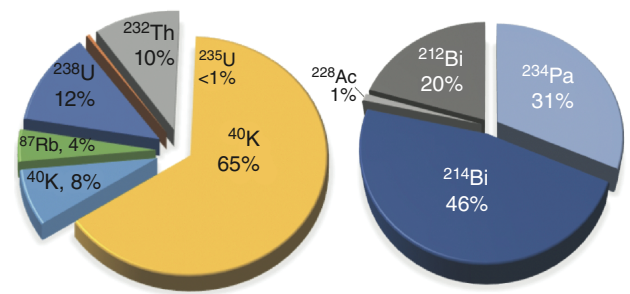
$$E_{\bar{\nu}_e}^{thr} = \frac{(M_n + m_e)^2 - M_p^2}{2M_p} = 1.806[MeV]$$
 (1.3)

assuming the laboratory frame (i.e., stationary target) and where M_p , M_n , and m_e are the masses of the proton (938.272 MeV), neutron (939.565 MeV), and electron (0.5110 MeV). The neutrino mass is unknown and contributes negligibly to this reaction. Although its upper limit is <0.8 eV/c^2 (Aker et al., 2022), estimates of the neutrino's mass is of the order of 10s–100s of meV (de Salas et al., 2018). This energy threshold restricts the detectable antineutrinos to β^- decays from the ²³⁸U and ²³²Th decay chains (Fig. 1.1).

1.3.1. Technical Details for Detecting Geoneutrinos

Here, we highlight some relevant aspects of the detection scheme.

Detection occurs when an antineutrino interacts with a free proton, transforming it to a neutron plus a positron, which then causes two flashes of light close in space and time. Each flash of light occurring in these large liquid scintillation spectrometers, which are sited



Earth's geoneutrino contributors

Detectable geoneutrinos

Figure 1.1 Relative proportions of the Earth's present-day flux of naturally occurring geoneutrinos (left) and the detectable geoneutrinos (right) from the 232 Th decay chain (gray; 228 Ac and 212 Bi) and 238 U decay chain (blue; 234 Pa and 214 Bi, not shown is the negligible contribution from 212 Tl) (see also Table 1.2). 40 K has two branches: $β^-$ to 40 Ca (65%) and *EC* to 40 Ar (8%).





^b DM = Depleted Mantle, the chemically depleted source of MORB (mid-ocean ridge basalts), which is viewed as the chemical complement to the continental crust.

^c EM = Enriched Mantle, a smaller (e.g., $\frac{1}{5}$ mass), deeper, and more chemically enriched source of OIB (ocean island basalts).

^d From PREM, assuming a uniform surface crust of 24 km.

^e Using a LITHO1.0 model, see Table 1 in Wipperfurth et al. (2020).



NEUTRINO GEOSCIENCE: REVIEW, SURVEY, FUTURE PROSPECTS 7

Table 1.2 Detectable \overline{v}_e Events

β^- decay	$\overline{\nu}_e$ Max E^a	Branching	Max IBD cross–section ^b	% of total ^c
events	(MeV)	fraction	$\sigma_{IBD} \ (10^{-43} \ {\rm cm}^2)$	$\overline{\nu}_e$ signal
		²³² Th decay chain		
$^{228}\text{Ac} \rightarrow ^{228}\text{Th}$	2.134	1.00	4.3	1
$^{212}\text{Bi} \rightarrow ^{212}\text{Po}$	2.252	0.64	4.8	20
		²³⁸ U decay chain		
$^{234}\text{Pa} \rightarrow ^{234}\text{U}$	2.197	1.00	4.6	31
$^{214}\text{Bi} \rightarrow ^{214}\text{Po}$	3.270	1.00	33	46
$^{212}\text{TI} \rightarrow ^{212}\text{Po}$	4.391	0.0002	90	<<1%

^a There is a spectrum of energies for each antineutrino generated during a β^- decay, where typically the $\overline{\nu}_e$ takes about $\frac{2}{3}$ and the e^- about $\frac{1}{3}$ of the reaction energy (Q).

1–2 km underground to shield them from descending, atmospherically produced muons, are detected by the thousands of photomultiplier tubes covering the inner walls, each facing the detector's central volume.

Energy conservation requires that $E_{\overline{\nu}_e} + M_p = T_{e^+} +$ $m_e + M_n + T_n$, with T_{e^+} and T_n being the kinetic energy of the positron and neutron. The prompt event involves the positron being annihilated in picoseconds by an electron, with the signal being the sum of the reaction releasing a 1.022 MeV energy flash (the sum of the masses of these two leptons) plus the characteristic kinetic energy inherited by the positron from the antineutrino $(E_{prompt} = (E_{\overline{\nu}_e} + M_p - m_e - M_n - T_n) + 2m_e$, or $= E_{\overline{\nu}_e} - T_n - 0.782$ [MeV]). The accompanying emitted neutron undergoes a cascade of collisions (thermalizing events, loss of energy to its surroundings as it goes toward thermal equilibrium) over about 200 µs and approximately 15 cm from the initial interaction point. This neutron is ultimately captured by a second free proton creating ²H, resulting in a 2.22 MeV (binding energy) flash. This rare event sequence is eminently detectable because of its characteristics: two flashes of light in space and time, with the second flash having a specific energy. This reaction chain eliminates most background and improves the signal to noise ratio by a million-fold.

The organic liquid scintillator is mostly a long chain, aromatic ring hydrocarbon with approximately an H:C proportion of \sim 2. A wavelength shifting fluor compound is added to the scintillator to set the fluorescence peak emission at \sim 350–400 nm in order to reach the maximum quantum efficiency of the photomultiplier tubes. The photon yield for the liquid scintillator is typically a light yield of 200–400 photons/MeV.

The interaction cross-section of antineutrinos (and neutrinos) scales with their energy. For each β^- decay,

there is a spectrum of \overline{v}_e emitted energies, which in turn means a spectrum of interaction cross-sections. For IBD detection (i.e., starting at 1.806 MeV), the probability of a geoneutrino detection is low (order $1/10^{19}$), given that their cross-sections are between 10^{-48} and 10^{-46} m² (Vogel & Beacom, 1999). The overall emission above the energy threshold level are $0.40~\mathrm{U}~\bar{\nu}_e$ per decay and $0.156~\mathrm{Th}~\bar{\nu}_e$ per decay. There are four decay chains which produce detectable antineutrinos: two from the $^{232}\mathrm{Th}$ and two from the $^{238}\mathrm{U}$ decay chains (Table 1.2). The BSE has a Th/U mass ratio of 3.77 (or molar Th/U = 3.90) (Wipperfurth et al., 2018). However, despite Th being four times more abundant than U, attributes of the IBD detection method (i.e., $E_{\bar{\nu}_e}$, branching fraction, and σ_{IBD}) make U much easier to detect.

1.3.2. Detectors: Existing, Being Built, Being Planned

Currently, there are two detectors (Fig. 1.2) measuring the Earth's geoneutrino flux: KamLAND (1 kt), in Kamioka, Japan (Araki et al., 2005; Watanabe, 2019), and SNO+ (1 kt) in Sudbury, Ontario, Canada (Andringa et al., 2016), experiments. The Borexino detector (0.3 kt), in Gran Sasso, Italy (Agostini et al., 2020), has finished. The JUNO (20 kt) experiment in Jiangmen, Guangdong province, China (An et al., 2016), is currently being built. The Jinping (~4 kt) experiment in Jinping Mountains, Sichuan province, China (Beacom et al., 2017), is in development, with prototype detectors onsite testing future detector materials and technologies. Detectors in the proposal stage include Baksan in the Caucasus mountains in Russia (Domogatsky et al., 2005), Andes in Agua Negra tunnels linking the borders of Chile and Argentina (Dib et al., 2015), and a proposed ocean bottom detector

^b As the energy of the antineutrino decreases so does its interaction cross-section.

^c Numbers from Tables 3 and 5 in Fiorentini et al. (2007).

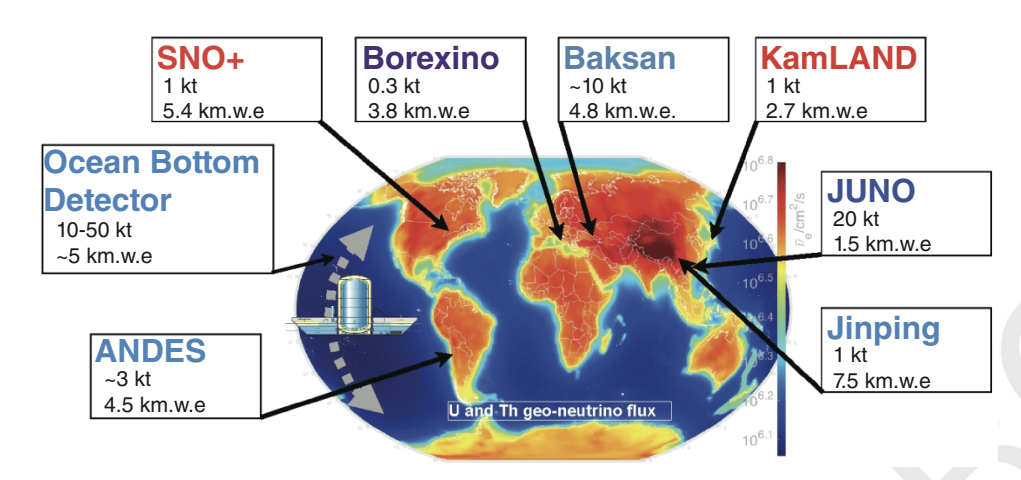


Figure 1.2 Present-day global distribution of detectors counting geoneutrino (red), have counted (purple), and are in the development and/or planning stage (blue). JUNO (bold blue) is in the construction phase. Background figure is the calculated global geoneutrino flux (order $10^6 \ \overline{\nu}_e \ cm^{-2} \ s^{-1}$) (Usman et al., 2015); the relatively high flux density seen in the Himalayas is directly correlated with its greater crustal thickness.

(OBD). Significantly, the Andes detector is the only proposed detector to be sited in the Southern Hemisphere.

There are ongoing developments for a ocean-going detector. A team of particle physicists from the University of Hawaii put forth a proposal more than 10 years ago for an OBD called Hanohano (Learned et al., 2007). A team of Japanese particle physicists and engineers and Earth scientists from JAMSTEC (Japan Agency for Marine-Earth Science and Technology) are currently moving forward with a project to deploy and test a mobile prototype detectors ("Ocean Bottom Detector" (OBD) scale is not yet set, but envisaged to up to 1 ton) off the coast of Japan. A mobile ocean-going detector offers a complementary measurement to land-based experiments. By sitting in the middle of the Pacific Ocean, 3,000 km from South America, 3,000 km from Australia, and ~3.000 km from the core-mantle boundary, such a detector gets a "mostly-mantle" signal.

1.4. LATEST RESULTS FROM THE PHYSICS EXPERIMENTS

Results from the physics experiments follow counting statistics, with increasing exposure (time spent counting) uncertainties reduce. These experiments are attentive to systematic and statistical uncertainties and addressed these issues in great detail in their publications.

The measured geoneutrino flux is reported in $\bar{\nu}_e$ cm⁻² μs^{-1} for the KamLAND experiment and in TNU (Terrestrial Neutrino Unit) for the Borexino experiments. Mantovani et al. (2004) introduced TNU as a way to normalize the differences between detectors. A 1 TNU signal represents the detection of one event in a 1 kiloton

liquid scintillation detector over a one-year exposure with a 100% detection efficiency. A 1 kiloton liquid scintillation detector has $\sim 10^{32}$ free protons (the detection target). Each detector has its own efficiency relative to a 1 kiloton fiducial volume detector, which accounts for the differences in the size of detector, its photomultiplier coverage, its response efficiency of the scintillator, and other factors. The conversion factor between signal in TNU and flux in $\overline{\nu}_e$ cm $^{-2}$ μ s $^{-1}$ depends on the Th/U ratio and has a value of 0.11 $\overline{\nu}_e$ cm $^{-2}$ μ s $^{-1}$ TNU $^{-1}$ for Earth's Th/U $_{molar}$ of 3.9.

The most recent results for the KamLAND and Borexino experiments are 32.1 ± 5.0 (Watanabe, 2019) and $47.0^{+8.4}_{-7.7}$ (Agostini et al., 2020) TNU, respectively. The SNO+ detector began counting in 2020 with a partial filled volume (with delays due to the covid-19 pandemic) and is yet to report their data.] The conversion between TNU and TW depends on the geological model assumed for the distribution of Th and U. Using geological models developed for both experiments, the radiogenic heating of the Earth ranges from 14 to 25 TW for Kam-LAND and 19 to 40 TW for Borexino (McDonough et al., 2020; Wipperfurth et al., 2020). The combined KamLAND and Borexino results mildly favors an Earth model with 20 TW present-day total power. Development of these and others geological models for each experiment are discussed later.

1.5. COMPOSITIONAL MODELS FOR THE EARTH

Earth scientists estimate the planet's radiogenic power within the bounds of 20 ± 10 TW (10^{12} watts), with many favoring estimates between 15 and 25 TW. In contrast, estimates from particle physics experiments (including a 19% contribution from K, not measured) range from





15.3^{+4.9}_{-4.9} TW (KamLAND, Japan) (Watanabe, 2019) to 38.2^{+13.6}_{-12.7} TW (Borexino, Italy) (Agostini et al., 2020). The latter estimate exceeds most predictions by geologists and so one might dismiss such finding from this emerging

and so one might dismiss such finding from this emerging field of science. The rub here, however, is that this broad range of TW estimates from particle physicists is mostly due to geological uncertainties associated with characterizing the surrounding ~ 500 km of lithosphere upon which these detectors are sited. These local lithologies contribute $\sim 40\%$ of the signal seen at a detector (Araki

et al., 2005; Wipperfurth et al., 2020).

Once a geoneutrino flux is measured at a detector, a geological model for the immediately surrounding ~500 km of continental crust is applied. This model is coupled with a model for the global lithosphere and mantle contributions (see Huang et al., 2013, for method details). Given that a detector's sensitivity scales with 1/distance², each experiment is most sensitive to the local flux. By taking the total measured signal and subtracting the contributions from the lithosphere (with all of its unknowns), the mantle's contribution to the planetary radiogenic power is identified. Because of its low abundances of Th and U relative to the continental crust (i.e., ng/g vs. μ g/g), the mantle's $\overline{\nu}_e$ contribution can be approximated as relatively homogeneous globally, with mantle heterogeneities in the signal being of the order 10–15% of its total signal (Šrámek et al., 2013).

There are three major models that predict the composition of the BSE, and thus the bulk Earth. In general, these models agree that the core has a negligible role in hosting the HPE. Although the Earth's core is often invoked as a host for radioactive HPE, mostly to power the geodynamo, there is a little support for such speculations. Recently, Wipperfurth et al. (2018) show that a maximum of <0.5% of the Earth's budget of Th and U could be hosted in the core. Petrologists have identified K-bearing sulfides that might have been extracted into the Earth's core. However, this evidence does not demonstrate the existence of potassium in the core, it only allows for its possibility. Such plausibility arguments need to be coupled with corroborating paragenetic evidence that is also free of negating geochemical consequences. In all instances, the extraction of a K-bearing phase into the core is not supported by other geochemical observations (e.g., no evidence for a range of alkali metals and refractory elements [Ca, REE] in the core). Finally, particle physics experiments have focused on the question of a nuclear reactor in the center of, or the surrounding, the Earth's core. Conclusions of these studies limit the power of a geological reactor to <3.7 TW (Gando et al., 2013) and <2.4 TW (Agostini et al., 2020) at the 95% confidence

The three major models can be characterized by their relative heat production (H): low H, medium H, and

high H. Heat production models range from 10 to 38 TW, assumes Th/ $U_{molar} = 3.90$ and K/U = 14,000 (Arevalo et al., 2009; Wipperfurth et al., 2018), and have relative heat contributions of $\sim 20\%$ from K, $\sim 40\%$ from Th, and ~40% from U (McDonough et al., 2020). Given these ratios there is a simple multiplier for these model compositions: a 20 TW model has 20 ng/g U (a 10 TW model has 10 ng/g U), 77 ng/g Th, and 280 µg/g K. Both Th and U are refractory lithophile elements, like Al, Ca, Ti, and the REE. Also, the Earth has been demonstrated multiple times through elemental and isotopic data to be chondritic (McDonough & Sun, 1995; Willig et al., 2020). Therefore, if we know the absolute abundance of one of these elements (e.g., U) in the bulk Earth, then we know the abundances of all 36 (e.g., assuming 20 ng/g U in the BSE and $(Al/U)_{chondritic} = 1.08 \times 10^6$, then $Al_{BSE} = 21.7 \text{ mg/g}$.

The low H models typically have heat production levels of about 10 TW. Models like Javoy et al. (2010) and Faure et al. (2020) have 11 TW of radiogenic power, and their refractory lithophile elements abundances in the BSE are enriched by 1.5 times CI chondrite. This enrichment factor is equivalent to core separation, meaning their bulk Earth model has a CI chondrite refractory element composition. Many of the low H models were constructed to explain a putative ¹⁴²Nd isotope anomaly for the Earth (Boyet & Carlson, 2005). Other low H to intermediate H models for the Earth invoke non-chondritic refractory element abundances due to collisional erosion processes, which involved losing a substantial fraction of the early Earth's crust (Campbell & O'Neill, 2012; Jackson & Jellinek, 2013; O'Neill & Palme, 2008). Advocates for these models have largely fallen silent, as a simpler explanation for the ¹⁴²Nd isotope anomaly became obvious (Bouvier & Boyet, 2016; Burkhardt et al., 2016). Finally, a consequence of the low H model is that the mantle has very little radiogenic power. Assuming a BSE with about 10 TW of radiogenic power and the continental crust contains $7.1_{-1.6}^{+2.1}$ TW (Table 1.3), then the mantle has only ~3 TW of radiogenic power and thus the dominant driver of the major geodynamic processes is primordial

The high H models typically have heat production levels of \geq 30 TW. Compositional models proposed by Turcotte et al. (2001) and Agostini et al. (2020) conclude the BSE as having 30–38 TW of radiogenic power. These models have no parallels in the cosmochemistry of meteorites. They predict that the bulk Earth is enriched in refractory lithophile elements by a factor of 2.5–3.2 × CI chondrite. A survey of chondritic meteorites documents enrichment factors for refractory elements ranging from 1 to 2.2 × CI (Alexander, 2019a, 2019b). In opposition to low H models, the high H models have radiogenic energy as dominantly driving the Earth's geodynamic processes.





 Table 1.3 Heat Producing Elements in the Continental Crust

Citationa	Model	s of the	continen	tal crust	BSE model
Estimates of uncertainty	1 (±30%)	2 low	2 high	3 (±35%)	4 (±10%
U (μg/g) in bulk Cont. crust	1.3	1.09	1.33	1.27	0.020
Th (μg/g) in bulk Cont. crust	5.6	4.20	5.31	5.64	0.077
K (μg/g) in bulk Cont. crust.	15,000	11,900	18,800	11,700	280
Heat production (nW/kg)	0.325	0.253	0.333	0.312	0.005
Heat production $(\mu W/m^3)^b$	0.943	0.733	0.967	0.906	0.023
Radiogenic power (TW) ^c	7.2	5.7	7.4	7.1	20
% total U in CC	36%	30%	37%	36%	_
% total Th in CC	40%	30%	38%	40%	_
% total K in CC	29%	23%	37%	23%	_

^a 1 = Rudnick and Gao (2014), 2 = Hacker et al. (2015),

Most *medium H* models have heat production levels of 20 ± 5 TW (McDonough & Sun, 1995; Palme & O'Neill, 2014), have enrichments in refractory elements consistent with that seen in chondritic meteorites, and are built from a residuum-melt relationship between peridotites (mantle rocks) and basalts (partial melts of the mantle). The BSE's composition comes from the least melt-depleted peridotites. This compositional model applies to the whole mantle and does not envisage any compositional layering (e.g., upper versus lower mantle domains). Moreover, this conclusion is supported by tomographic images of subducting oceanic slabs that penetrate into the lower mantle, documenting mass transfer between the upper and lower mantle and by inference whole mantle convection. In addition, the methodology used also captures into the primitive composition any potential domains that might have been created in the early Earth and since been isolated. Medium H models have approximately $\frac{2}{3}$ primordial and $\frac{1}{3}$ radiogenic energy driving the Earth's major geodynamic processes (i.e., mantle convection, plate tectonics, and the geodynamo). Recently, Yoshizaki and McDonough (2021) also showed that the Earth and Mars are equally enriched in refractory elements by $1.9 \times CI$, which might reflect the enrichment levels for

all of the terrestrial planets and point to a fundamental attribute of inner solar system's building blocks.

1.6. THE GEOLOGICAL PREDICTIONS

All of our models depend upon an accurate description of the abundances and distribution of Th and U in the continents. The role of the geologist in collaboration with neutrino scientists is to determine this spatial distribution of the HPE (Huang et al., 2013). Although this task is relatively straightforward, it offers many challenges and foremost among them are the difficulties in defining the structure and composition of rocks in the crust beneath the surface, particularly in areas where detectors are sited. Global scale models predicting the composition of the continental crust are available (Hacker et al., 2015; Rudnick & Gao, 2014; Sammon & McDonough, 2021; Wipperfurth et al., 2020); however, differences in these models lead to differences in their geoneutrino signal (Enomoto et al., 2007; Huang et al., 2013; Mantovani et al., 2004).

Wipperfurth et al. (2020) showed that geophysical characterization of the continental crust, using global seismic models, CRUST 2.0, CRUST 1.0, and LITHO1.0, did not significantly contribute to the uncertainty in models describing the distribution of the HPEs in the Earth. In contrast, however, the geochemical models were identified as contributing the greatest uncertainty to the model. This finding places the onus of responsibility squarely in the camp of the geochemists and the geologists in terms of understanding the 3-D distribution of lithologies and compositions within the crust.

The total geoneutrino signal represents contributions of three components (Fig. 1.3): Near-field crust (~40%), Far-field crust (~35%, i.e., the global lithospheric signal), and Mantle signals (~25%) (Wipperfurth et al., 2020). Paramount in modeling the measured signal at a detector is understanding the contribution from the closest ~500 km of lithosphere adjacent to the detector (i.e., 250 km outward in any direction from the detector). This region is often referred to as the Near-field, local, or regional crustal signal. This part of the continental crust, and particularly the upper crust, is the region of greatest interest, because of the relative separation distance between source neutrino emitter and the detector, and because it is the brightest geoneutrino emitter due to geological processes that concentrate the HPEs upward in the continental crust.

On average the continental crust is enriched in the HPE by more than a factor of 60 over the BSE and >100 over the present-day abundances in the modern mantle. Moreover, the upper part of the crust is 10 times enriched in the HPE as compared to the lower crust (Hacker et al., 2015; Rudnick & Gao, 2014; Sammon & McDonough, 2021;



^{3 =} Wipperfurth et al. (2020), and 4 = McDonough and Sun (1995), Arevalo et al. (2009), Wipperfurth et al. (2018).

^b Assumes average ρ (density) is 2,900 kg/m³ for the continental crust and 4,450 kg/m³ for the BSE.

^c See Table 1.1 for reservoir masses.

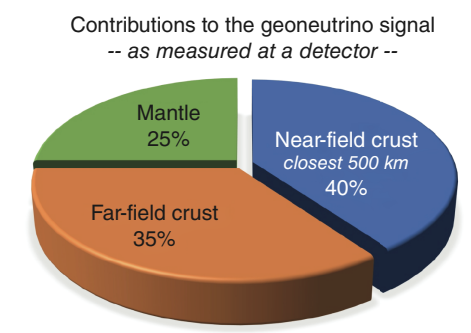


Figure 1.3 The relative contributions to the total geoneutrino signal: Near-field crust (out to 250 km in all directions), Far-field crust (the rest of the crust around the globe), and Mantle. The local and global Continental Lithospheric Mantle (CLM) contributes ~1 TNU or ~2% to the total geoneutrino signal at most detector sites.

Wipperfurth et al., 2020). Bulk compositional estimates of the continental crust report that it hosts about 30–40% of the HPEs in the BSE (Table 1.3).

The estimated model compositions of the continental crust (Table 1.3) come with a considerable amount of uncertainty in their predicted abundances. Importantly, all of these models consider the upper crust to represent about the top third of the continent's mass and assume a shared upper crustal compositional model (Rudnick & Gao, 2014), which dominates the geoneutrino flux. Using the global geophysical models that describe the continental crust (e.g., LITHO1.0) and a global model for the composition of the continents (Table 1.3), the geoneutrino signal for the Far-field crust (i.e., the crust minus the local contribution at the detector) ranges from ~8 to 19 TNU, depending on the local setting (Wipperfurth et al., 2020); locations like KamLAND and JUNO, near the coast, fall on the lower end of the scale, whereas locations like Jinping and SNO+, surrounded by a significant amount of continental crust, fall on the high end of the range. Wipperfurth et al. (2020) showed that when combining the data for KamLAND and Borexino and using their geological models found a mantle signal of 9.2 ± 8.5 TNU and found the Earth's global radiogenic power to be 21.5 ± 10.4 TW.

The lithospheric signal can be treated globally, but the local lithospheric signal is best done with a detail analysis of the geological, geochemical, and geophysical data of the region. Using this combination of data, one can build a 3-D model of the chemical and physical attributes of the local lithosphere. It is noteworthy, however, that such attempts have been conducted at both the Kam-LAND and Borexino experiment locations. Figure 1.4 and Table 1.4 present the range of predicted results for the geoneutrino flux at KamLAND, Borexino, and other locations.

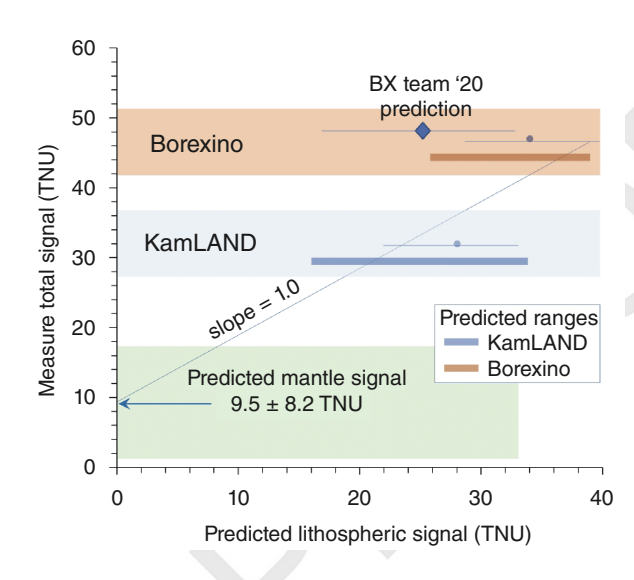


Figure 1.4 Model predictions for the geoneutrino signal at KamLAND and Borexino and predicted mantle flux (i.e., ~12 TW). See Table 1.4 for data sources and references. KamLAND's measured flux from Watanabe (2019) (32.1 \pm 5.0 TNU, uncertainty shown as a light blue, horizontal band; y-axis only constraint). Borexino's measured flux from Agostini et al. (2020) (47.0^{+8.4}_{7.7} TNU, uncertainty shown as a light orange, horizontal band; y-axis only constraint). The slope = 1 is because its a two-component system (crust + mantle). Estimated signals at future detector locations (Table 1.4) will better constrain the intercept (mantle prediction).

1.7. DETERMINING THE RADIOACTIVE POWER IN THE MANTLE

The particle physics experiment, at its simplest level, reports the geoneutrino flux at a detector. With this number in hand, along with a model for the local and global lithospheric contribution, the physicist then determines the planetary geoneutrino flux and the flux from the mantle. This idea was first laid out by Krauss et al. (1984). Later, Raghavan et al. (1998), in a comparative analyses of signals from detectors in continental and oceanic settings, specifically developed a scheme to determine the mantle flux.

Surface heat flux observations constrain the Earth to radiating 46 ± 3 TW (i.e., 0.09 W/m²). Based on a compositional model for the continental crust (Table 1.3), it contains about $7.1_{-1.6}^{+2.1}$ TW of radiogenic power, leaving ~40 TW as a mantle flux contribution. This latter flux contains contributions from the core (basal heating), which is estimated to be order 10 ± 5 TW, and mantle (i.e., order 30 \pm 5 TW, which includes radiogenic and primordial additions). A combined analysis of the Kam-LAND and Borexino results yields a mantle signal of 13 ± 12 TW (Wipperfurth et al., 2020). Consequently, a

Table 1.4 Geological Estimates of the Signal Contributions at Various Antineutrino Detectors

Detector	Reference	Total signal	Global crustal contribution	FFC	NFC	Mantle contribution ^a
KamLAND	(Enomoto et al., 2007)	38.5	28.2	10.5	17.7	10.3
KamLAND	(Huang et al., 2013)	30.7	20.6	7.3	13.3	8.8
KamLAND	(Fiorentini et al., 2012)	_	26.5	8.8	17.7	-
KamLAND	(Wipperfurth et al., 2020)	37.9	27.0	8.8	18.2	9.4
Borexino	(Huang et al., 2013)	43.5	29.0	13.7	15.3	8.7
Borexino	(Coltorti et al., 2011)	43.5	26.2	16.0	10.2	9.9
Borexino	(Fiorentini et al., 2012)	_	25.3	15.7	9.7	-/
Borexino	(Agostini et al., 2020)	47.0	25.5	16.3	9.2	20.6
Borexino	(Wipperfurth et al., 2020)	43.9	32.5	14.8	18.2	9.4
SNO+	(Huang et al., 2014)	40.0	30.7	15.1	15.6	7.0
SNO+	(Strati et al., 2017)	43.1	30.5	15.2	15.3	6.9
SNO+	(Wipperfurth et al., 2020)	46.8	34.3	14.7	19.6	9.1
JUNO	(Strati et al., 2015)	39.7	28.2	13.4	17.4	8.8
JUNO	(Gao et al., 2020)	49.1	38.3	9.8	28.5 ^b	8.7
JUNO	(Wipperfurth et al., 2020)	40.5	29.8	12.7	17.1	9.5
Jinping	(Šrámek et al., 2016)	58.5	50.3	18.7	31.6	8.2
Jinping	(Wan et al., 2017)	59.4	49.0	_	_	10.4
Jinping	(Wipperfurth et al., 2020)	60.0	49.0	18.7	30.3	9.3
Hanohano	(Huang et al., 2013)	12.0	2.6	2.6	_	9.0

Notes: All numbers are reported in units of TNU (see text for details).

large range of compositional models are acceptable for the Earth's radiogenic power (e.g., Table 1.4).

An important step toward reducing the uncertainties on the estimated mantle radiogenic power would be either (1) determine the mantle flux in oceanic setting and/or (2) improve the accuracy and precision of the local signal (Near-field). In the next section, we address measuring the signal with an OBD. Here, we consider differences in estimates of the local signal.

Figure 1.4 and Table 1.4 illustrate the problem. The graph is designed to extract the mantle signal from the combined analysis of data from different detectors. The signal is made up of crust plus mantle; it is a two-component only system (i.e., slope = 1). The mantle signal (the ordinate intercept) can be considered, at this scale, homogeneous. Note, Šrámek et al. (2013) found that even when modeling a mantle with two large, approximately antipodal structures (e.g., LLSVP: Large low shear velocity provinces), which might contain a factor of five or more difference in K, Th, and U abundances, the global mantle signal varied by only $\pm 10\%$. Thus, the

mantle flux estimate highly depends on the accuracy of the crustal predictions for each detector.

Figure 1.4 also reveals the challenge with different model predictions for the geoneutrino flux from the bulk lithosphere; each model and their uncertainties yield different geoneutrino flux estimates, and in turn this influences the prediction for the mantle signal. It is unclear which model provides a more accurate representation of the crust. In 2020, the Borexino particle physics team reported an updated prediction for the local lithospheric signal and mantle (Agostini et al., 2020), which leads to their distinctly higher prediction (and large uncertainty) for the Earth's total radiogenic power (i.e., $38^{+13.6}_{-12.7}$ TW). Thus, a clear challenge for the geological community is to independently construct a 3-D model for the local lithosphere and from this predict a geoneutrino flux. By doing so, it would test this hypothesized lithospheric model constructed by the particle physics team and their markedly radiogenic prediction for the Earth's HPE abundances.

Future geoneutrino detectors are being built at locations in Guangzhou, China (JUNO), and the eastern

^a Reported or calculated flux. NFF = Near-field Crust contribution, FFC = Far-field crust contribution.

^b Authors defined the JUNO NFC as $10^{\circ} \times 10^{\circ}$. The flux contribution from the CLM (Continental Lithospheric Mantle) is not included, as it is not always reported by authors; its contribution is typically on the order of 1 to 2 TNU.

slope of the Tibetan plateau (Jinping). Each location has already had a geological model prediction of their geoneutrino signal, which critically depends upon the modeling of the local lithospheric signal (i.e., crust plus lithospheric mantle). The challenge faced by the geological community is how to treat differences in the production of the local lithospheric signal. Recently, Strati et al. (2015) and Gao et al. (2020) reported their predicted both crust signal for the JUNO detector as $28.2^{+5.2}_{-4.5}$ TNU and 38.3 ± 4.8 TNU, respectively. These numbers do not overlap with their combined uncertainties and challenge us to resolve this difference. Consequently, the physics experiments are bringing further insights into our understanding of the HPE in the Earth, which are forcing geologists to improve their 3-D physical and chemical descriptions of the Earth.

The question remains – how to critically assess the accuracy of these competing predictions? Some insights will come by adding more detectors and comparing multiple signals in order to predict a mantle signal. The SNO+ detector has begun counting and so we look forward to adding that data point to Figure 1.4 in the near future.

1.8. FUTURE PROSPECTS

The signal at all of these detectors depends critically upon the signal from the local lithosphere. Given two unknowns parameters (crust and mantle), then the problem is reduced to identifying exclusively the mantle signal. The best way to determine the mantle signal is to detect it far away from continental sources. This means determining the mantle geoneutrino flux from the deep ocean basin likely somewhere in the central Pacific Ocean. An ideal location in the central southern Pacific that is approximately a core – mantle distance (~3,000 km) away from continental masses rimming the Pacific.

The idea of an ocean-going detector that could isolate the mantle signal was introduced by Raghavan et al. (1998). In 2007, the Hanohano project (Learned et al., 2007) provided a detailed technical report showing that an ocean-going neutrino detector could be deployed in the deep ocean and serve multiple applications. Šrámek et al. (2013) identified a series of target locations in a north-south transit through the Pacific that could map out potential mantle structures and identify compositional heterogeneities in the deep mantle.

The concept envisages an ocean-going geoneutrino detector that is deployed on a yearly basis, anchored just above the ocean floor, recovered, serviced, and redeployed. Such a detector would be able to measure the mantle geoneutrino flux over multiple deployments. Given a small lithospheric signal from the Far-field continents and the oceanic crust, it is estimated that 75% of the signal measured by an OBD would be from the mantle.

Table 1.5 Estimated One-year Signals and Backgrounds for 1.5 kt OBD by Detector Simulationa

Signals		Backgrounds			
			Rate ^b		
	Rateb		<8.5	<2.6 MeV	
Source	(mantle)	Source	MeV	(geo $\overline{\nu}_e$ region)	
U	7.4 (5.5)	Reactor \overline{v}_e	4.5	1.7	
Th	1.8 (1.3)	Accidental	1.8	1.8	
Total	9.2 (6.8)	⁹ Li, ⁸ He	6.2	0.6	
		$^{13}C(\alpha, n)^{16}O$	3.6	2.6	
		Total	16.1	6.7	

^a Simulation assumes the detector was deployed off the coast of Hawaii at 2.7 km depth. To reduce the radioactive background relative to the detector surface, a fiducial cut was applied (72 cm).

b Rate is in units of counted events/year.

Geoneutrino and reactor neutrino spectrum from Dye and Barna (2015).

Table 1.5 and Figure 1.5 summarize estimated signals and backgrounds for 1.5 kt OBD by detector simulation. The detector was assumed to be deployed off the coast of Hawaii at the depth of 2.7 km. Radioactive contamination in the detector components, such as liquid scintillator, acrylic vessel, photomultiplier tube, and its water pressure resistant vessel, can be the sources of the backgrounds (e.g., accidental and $^{13}C(\alpha,n)^{16}O$). Detector cleanness controls how much scintillator mass we can use as the fiducial volume. Seawater acts as a shield for cosmic-ray muons, which induces radioactive isotopes (e.g., ⁹Li, ⁸He). The deeper a detector can be anchored just above the seafloor, the greater the reduction in the muon-related background. A 1.5 kt OBD has sensitivity to measure mantle geoneutrino at 3.4σ level with three-year exposure measurement. A simple comparison between OBD and KamLAND (Watanabe, 2019), with both as 1.5 kt detectors, yields a geoneutrino flux of 7 [5] and 9 [24] events/year for mantle and non mantle (including the crust and other sources listed in Table 1.5) signals, respectively.

Such an instrument is capable of accurately determining the mantle geoneutrino flux, which in turn can be used to unravel the geological signals measured at land-based experiments. Given this, we would have the capability to interpret the local lithospheric signal from all of the existing and future detectors.

Neutrino Geoscience compares geoneutrino flux measurements from particle physics experiments with flux predictions derived from integrating data from geology, geophysics, and geochemistry. The particle physics

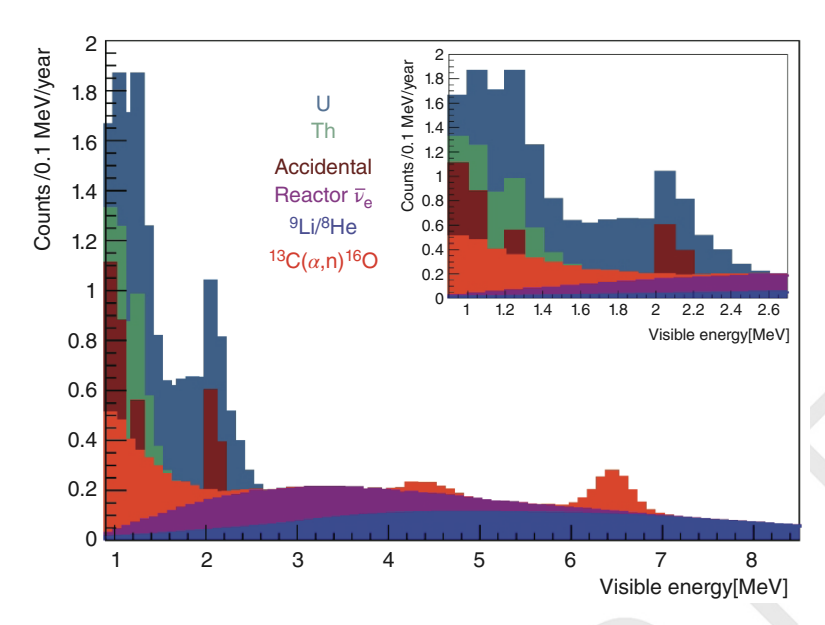


Figure 1.5 Expected energy spectrum of 1.5 kt OBD estimated by detector simulation. Right top panel focuses on geoneutrino energy range.

community are focusing on improving their measurement precision and detector technology. Efforts in geosciences are focused on improving our models for the abundance and distribution of the HPEs. Improvements in crustal studies are of greatest need. Global and regional geochemical studies, including studies of crustal terrains and xenoliths, can help constrain the composition of the deep crust.

Holistic approaches are essential for developing improved models of the crust. For example, considerable promise comes from studies that incorporate thermodynamic modeling (e.g., Perple_X; (Connolly, 2005)) with geochemical and seismic data, in combination with constraints from crustal geotherms (e.g., surface heat flux studies, curie depth maps, reflection data estimates on Moho temperatures, etc.), all in an effort to determine crustal compositional trends from the surface to the Moho (Sammon et al., 2020; Takeuchi et al., 2019). The other geological priority needing improvements is reducing or resolving the up to 30% spread in crustal predictions of the geoneutrino flux for all but the SNO+ experiment (Table 1.4).

AUTHOR CONTRIBUTIONS

Both authors discussed the concepts introduced in the chapter. The writing of the main text was principally conducted by WFM; both authors were involved in the calculations and editing process. The authors have read and approved this manuscript.

DATA AVAILABILITY STATEMENT

The data used in this manuscript is freely available upon request.

ACKNOWLEDGMENTS

W. F. McDonough gratefully acknowledges NSF grant support (EAR1650365 and EAR2050374). H. Watanabe gratefully acknowledges grants (JP15H05833 and JP20H01909) from the Japan Society for the Promotion of Science. W. F. McDonough and H. Watanabe appreciate review comments from many colleagues and are very thankful to the two anonymous reviewers and the editor handling our chapter. There are no financial or other conflicts of interest with this work.

REFERENCES

Agostini, M., Altenmüller, K., Appel, S., Atroshchenko, V., Bagdasarian, Z., Basilico, D., et al. (2020). Comprehensive geoneutrino analysis with Borexino. *Physical Review D*, *101*(1), 012009. doi: 10.1103/PhysRevD.101.012009

Aker, M., Beglarian, A., Behrens, J., Berlev, A., Besserer, U., Bieringer, B., et al. (2021). First direct neutrino-mass measurement with sub-eV sensitivity. *arXiv* preprint, arXiv:2105.08533.

Alexander, C. M. O. (2019a). Quantitative models for the elemental and isotopic fractionations in chondrites: The carbonaceous chondrites. *Geochimica et Cosmochimica Acta*, 254, 277–309. doi: 10.1016/j.gca.2019.02.008



- Alexander, C. M. O. (2019b). Quantitative models for the elemental and isotopic fractionations in the chondrites: The non-carbonaceous chondrites. *Geochimica et Cosmochimica Acta*, 254, 246–276. doi: 10.1016/j.gca.2019.01.026
- An, F., An, G., An, Q., Antonelli, V., Baussan, E., Beacom, J., et al. (2016). Neutrino Physics with JUNO. *Journal of Physics G: Nuclear and Particle Physics*, 43(3), 030401. doi: 10.1088/0954-3899/43/3/030401
- Andringa, S., Arushanova, E., Asahi, S., Askins, M., Auty, D. J., Back, A. R., et al. (2016). Current status and future prospects of the SNO+ experiment. *Advances in High Energy Physics*, 2016, 6194250. doi: 10.1155/2016/6194250
- Araki, T., Enomoto, S., Furuno, K., Gando, Y., Ichimura, K., Ikeda, H., et al. (2005). Experimental investigation of geologically produced antineutrinos with KamLAND. *Nature*, *436*(7050), 499–503. doi: 10.1038/nature03980
- Arevalo, R., McDonough, W. F., & Luong, M. (2009). The K/U ratio of the silicate Earth: Insights into mantle composition, structure and thermal evolution. *Earth and Planetary Science Letters*, 278(3–4), 361–369. doi: 10.1016/j.epsl.2008.12.023
- Beacom, J. F., Chen, S., Cheng, J., Doustimotlagh, S. N., Gao, Y., Gong, G., et al. (2017). Physics prospects of the jinping neutrino experiment. *Chinese Physics C* 41(2), 023002. doi: 10.1088/1674-1137/41/2/023002
- Bouvier, A., & Boyet, M. (2016). Primitive Solar System materials and Earth share a common initial ¹⁴²Nd abundance. *Nature*, *537*(7620), 399–402. doi: 10.1038/nature19351
- Boyet, M., & Carlson, R. W. (2005). ¹⁴²Nd evidence for early (>4.53 Ga) global differentiation of the silicate Earth. *Science*, *309*(5734), 576–581. doi: 10.1126/science.1113634
- Burkhardt, C., Borg, L. E., Brennecka, G. A., Shollenberger, Q. R., Dauphas, N., & Kleine, T. (2016). A nucleosynthetic origin for the Earth's anomalous ¹⁴²Nd composition. *Nature*, *537*(7620), 394–398. doi: 10.1038/nature18956
- Campbell, I. H., & O'Neill, H. S. C. (2012). Evidence against a chondritic Earth. *Nature*, 483(7391), 553–558. doi: 10.1038/nature10901
- Chambat, F., Ricard, Y., & Valette, B. (2010). Flattening of the Earth: Further from hydrostaticity than previously estimated: Hydrostatic flattening. *Geophysical Journal International*, 183(2), 727–732. doi: 10.1111/j.1365-246X.2010.04771.x
- Coltorti, M., Boraso, R., Mantovani, F., Morsilli, M., Fiorentini, G., Riva, A., et al. (2011). U and Th content in the Central Apennines continental crust: A contribution to the determination of the geo-neutrinos flux at LNGS. *Geochimica et Cosmochimica Acta* 75(9), 2271–2294.
- Connolly, J. A.D. (2005). Computation of phase equilibria by linear programming: A tool for geodynamic modeling and its application to subduction zone decarbonation. *Earth and Planetary Science Letters*, 236(1), 524–541. doi: 10.1016/j.epsl.2005.04.033
- Davies, J. H. (2013). Global map of solid earth surface heat flow. *Geochemistry, Geophysics, Geosystems* 14(10), 4608–4622. doi: 10.1002/ggge.20271
- de Salas, P. F., Gariazzo, S., Mena, O., Ternes, C. A., & Tórtola, M. (2018). Neutrino mass ordering from oscillations and beyond: 2018 status and future prospects. *Frontiers in Astronomy and Space Sciences*, 5, 36. doi: 10.3389/fspas.2018.00036

- Dib, C. O. (2015). ANDES: An underground laboratory in South America. *Physics Procedia*, 61, 534–541. doi: 10.1016/j.phpro.2014.12.118
- Domogatsky, G., Kopeikin, V., Mikaelyan, L., & Sinev, V. (2005). Neutrino geophysics at Baksan I: Possible detection of georeactor antineutrinos. *Physics of Atomic Nuclei*, 68(1), 69–72. doi: 10.1134/1.1858559
- Dye, S., & Barna, A. (2015). Global antineutrino modeling for a web application. (arXiv:1510.05633)
- Dziewonski, A. M., & Anderson, D. L. (1981). Preliminary reference Earth model. *Physics of the Earth and Planetary Interiors*, 25(4), 297–356. doi: 10.1016/0031-9201(81)90046-7
- Enomoto, S., Ohtani, E., Inoue, K., & Suzuki, A. (2007). Neutrino geophysics with KamLAND and future prospects. *Earth and Planetary Science Letters*, 258(1–2), 147–159. doi: 10.1016/j.epsl.2007.03.038
- Faure, P., Boyet, M., Bouhifd, M., Manthilake, G., Hammouda, T., & Devidal, J.-L. (2020). Determination of the refractory enrichment factor of the bulk silicate Earth from metal-silicate experiments on rare earth elements. *Earth and Planetary Science Letters*, 116644. doi: 10.1016/j.epsl.2020.116644
- Fiorentini, G., Fogli, G., Lisi, E., Mantovani, F., & Rotunno, A. (2012). Mantle geoneutrinos in KamLAND and Borexino. *Physical Review D*, 86(3), 033004. doi: 10.1103/Phys-RevD.86.033004
- Fiorentini, G., Lissia, M., & Mantovani, F. (2007). Geoneutrinos and earth's interior. *Physics Reports* 453(5–6), 117–172. doi: 10.1016/j.physrep.2007.09.001
- Gando, A., Gando, Y., Hanakago, H., Ikeda, H., Inoue, K., Ishidoshiro, K., et al. (2013). Reactor on-off antineutrino measurement with KamLAND. *Physical Review D*, 88, 033001. doi: 10.1103/PhysRevD.88.033001
- Gao, R., Li, Z., Han, R., Wang, A., Li, Y., Xi, Y., et al. (2020). JULOC: A local 3-D high-resolution crustal model in South China for forecasting geoneutrino measurements at JUNO. *Physics of the Earth and Planetary Interiors*, 299, 106409.
- Hacker, B. R., Kelemen, P. B., & Behn, M. D. (2015). Continental Lower Crust. Annual Review of Earth and Planetary Sciences, 43(1), 167–205. doi: 10.1146/annurev-earth-050212-124117
- Huang, Y., Chubakov, V., Mantovani, F., Rudnick, R. L., & McDonough, W. F. (2013). A reference Earth model for the heat-producing elements and associated geoneutrino flux. *Geochemistry, Geophysics, Geosystems*, 14(6), 2003–2029. doi: 10.1002/ggge.20129
- Huang, Y., Strati, V., Mantovani, F., Shirey, S. B., & McDonough, W. F. (2014). Regional study of the Archean to Proterozoic crust at the Sudbury Neutrino Observatory (SNO+), Ontario: Predicting the geoneutrino flux. *Geochemistry, Geophysics, Geosystems*, 15(10), 3925–3944. doi: 10.1002/2014GC005397
- Jackson, M. G., & Jellinek, A. M. (2013). Major and trace element composition of the high ³He/⁴He mantle: Implications for the composition of a nonchonditic earth. *Geochemistry, Geophysics, Geosystems*, *14*(8), 2954–2976. doi: 10.1002/ggge.20188
- Jaupart, C., Labrosse, S., Lucazeau, F., & Mareschal, J.-C. (2015). Temperatures, heat, and energy in the mantle of the Earth. In D. Bercovici (Ed.), *Mantle Dynamics* (Vol 7,





p. 223–270). Oxford Elsevier. Editor-in-chief G. Schubert doi: 10.1016/B978-0-444-53802-4.00126-3

16 CORE-MANTLE CO-EVOLUTION

- Javoy, M., Kaminski, E., Guyot, F., Andrault, D., Sanloup, C., Moreira, M., et al. (2010). The chemical composition of the Earth: Enstatite chondrite models. *Earth and Planetary Science Letters* 293(3), 259–268. doi: 10.1016/j.epsl.2010.02.033
- Krauss, L. M., Glashow, S. L., & Schramm, D. N. (1984). Anti-neutrinos astronomy and geophysics. *Nature*, *310*, 191–198. doi: 10.1038/310191a0
- Learned, J. G., Dye, S. T., & Pakvasa, S. (2007). Hanohano: A deep ocean anti-neutrino detector for unique neutrino physics and geophysics studies. In *Neutrino Telescopes. Proceedings, 12th International Workshop, Venice, Italy*, March 6–9, 2007 (p. 235–269). (arXiv:0810.4975)
- Mantovani, F., Carmignani, L., Fiorentini, G., & Lissia, M. (2004). Antineutrinos from Earth: A reference model and its uncertainties. *Physical Review D*, 69(1), 013001. doi: 10.1103 /PhysRevD.69.013001
- McDonough, W. F., & Sun, S. S. (1995). The composition of the Earth. *Chemical Geology*, *120*(3–4), 223–253. doi: 10.1016/0009-2541(94)00140-4
- McDonough, W. F., Šrámek, O., & Wipperfurth, S. A. (2020). Radiogenic power and geoneutrino luminosity of the Earth and other terrestrial bodies through time. *Geochemistry, Geophysics, Geosystems*, 21(7), e2019GC008865. doi: 10.1029/2019GC008865
- McDonough, W. F., & Yoshizaki, T. (2021). Terrestrial planet compositions controlled by accretion disk magnetic field.

 Progress in Earth and Planetary Science, on line. doi: 10.1186/s40645-021-00429-4
- O'Neill, H. S. C., & Palme, H. (2008). Collisional erosion and the non-chondritic composition of the terrestrial planets. *Philosophical Transactions of the Royal Society of London A: Mathematical, Physical and Engineering Sciences*, *366*(1883), 4205–4238. doi: 10.1098/rsta.2008.0111
- Palme, H., & O'Neill, H. S. C. (2014). Cosmochemical estimates of mantle composition. In R. W. Carlson (Ed.), *The Mantle and Core* (Vol. 3 of *Treatise on Geochemistry* (Second Edition), pp. 1–39). Oxford: Elsevier. (Editors-in-chief H. D. Holland and K. K. Turekian) doi: 10.1016/B978-0-08-095975-7.00201-1
- Raghavan, R. S., Schoenert, S., Enomoto, S., Shirai, J., Suekane, F., & Suzuki, A. (1998). Measuring the global radioactivity in the Earth by multidetector antineutrino spectroscopy. *Physical Review Letters*, 80(3), 635. doi: 10.1103/Phys-RevLett.80.635
- Rudnick, R. L., & Gao, S. (2014). Composition of the Continental Crust. In R. Rudnick (Ed.), *The Crust* (Vol. 4 of *Treatise on Geochemistry (Second Edition)*, p. 1–51). Elsevier. (Editors-in-chief H. D. Holland and K. K. Turekian) doi: 10.1016/B978-0-08-095975-7.00301-6
- Sammon, L., Gao, C., & McDonough, W. (2020). Lower crustal composition in the southwestern United States. *Journal of Geophysical Research: Solid Earth*, 125(3), e2019JB019011. doi: 10.1029/2019JB019011
- Sammon, L. G., & McDonough, W. F. (2021). A geochemical review of amphibolite, granulite, and eclogite facies lithologies: Perspectives on the deep continental

- crust. Earth and Space Science Open Archive, 37. doi: 10.1002/essoar.10506164.1
- Śrámek, O., McDonough, W. F., Kite, E. S., Lekić, V., Dye, S. T., & Zhong, S. (2013). Geophysical and geochemical constraints on geoneutrino fluxes from Earth's mantle. *Earth and Planetary Science Letters*, 361, 356–366. doi: 10.1016/j.epsl.2012.11.001
- Šrámek, O., Roskovec, B., Wipperfurth, S. A., Xi, Y., & McDonough, W. F. (2016). Revealing the Earth's mantle from the tallest mountains using the Jinping Neutrino Experiment. *Scientific Reports*, 6(1), 33034. doi: 10.1038/srep33034
- Strati, V., Baldoncini, M., Callegari, I., Mantovani, F., McDonough, W. F., Ricci, B., et al. (2015). Expected geoneutrino signal at JUNO. *Progress in Earth and Planetary Science*, 2(1)1–7. doi: 10.1186/s40645-015-0037-6
- Strati, V., Wipperfurth, S. A., Baldoncini, M., McDonough, W. F., & Mantovani, F. (2017). Perceiving the crust in 3-D: A model integrating geological, geochemical, and geophysical data. *Geochemistry, Geophysics, Geosystems*, 18(12), 4326–4341. doi: 10.1002/2017GC007067
- Takeuchi, N., Ueki, K., Iizuka, T., Nagao, J., Tanaka, A., Enomoto, S., et al. (2019). Stochastic modeling of 3-D compositional distribution in the crust with Bayesian inference and application to geoneutrino observation in Japan. *Physics of the Earth and Planetary Interiors*, 288, 37–57. doi: 10.1016/j.pepi.2019.01.002
- Turcotte, D. L., Paul, D., & White, W. M. (2001). Thorium-uranium systematics require layered mantle convection. *Journal of Geophysical Research: Solid Earth*, *106*(B3), 4265–4276. doi: 10.1029/2000JB900409
- Usman, S. M., Jocher, G. R., Dye, S. T., McDonough, W. F., & Learned, J. G. (2015). AGM2015: Antineutrino Global Map 2015. *Scientific Reports* (51)13945.doi: 10.1038/srep13945
- Vogel, P., & Beacom, J. F. (1999). Angular distribution of neutron inverse beta decay, $\overline{\nu}_e + p \rightarrow e^+ + n$. *Physical Review D*, 60(5), 053003. doi: 10.1103/PhysRevD.60.053003
- Wan, L., Hussain, G., Wang, Z., & Chen, S. (2017). Geoneutrinos at Jinping: Flux prediction and oscillation analysis. *Physical Review D*, *95*, 053001. doi: 10.1103/PhysRevD.95.053001
- Watanabe, H. (2019). *Geo-neutrino measurement with Kam-LAND*. Presentation at "Neutrino Geoscience 2019 Prague", Czech Republic, October 21–23. Retrieved from https://indico.cern.ch/event/825708/contributions/3552210/
- Willig, M., Stracke, A., Beier, C., & Salters, V. J. M. (2020). Constraints on mantle evolution from Ce-Nd-Hf isotope systematics. *Geochimica et Cosmochimica Acta*, 272, 36–53. doi: 10.1016/j.gca.2019.12.029
- Wipperfurth, S. A., Guo, M., Šrámek, O., & McDonough, W. F. (2018). Earth's chondritic Th/U: Negligible fractionation during accretion, core formation, and crust–mantle differentiation. *Earth and Planetary Science Letters*, 498, 196–202. doi: 10.1016/j.epsl.2018.06.029
- Wipperfurth, S. A., Šrámek, O., & McDonough, W. F. (2020). Reference models for lithospheric geoneutrino signal. *Journal of Geophysical Research*, *125*(2), e2019JB018433. doi: 10.1029/2019JB018433
- Yoshizaki, T., & McDonough, W. F. (2021). Earth and Mars–distinct inner solar system products. *Geochemistry 81*, 125746. doi: 10.1016/j.chemer.2021.125746







Author Queries

AQ1	please provide volume and page range details
AQ2	please provide place of publication details.
AQ3	please provide page range details.

